https://doi.org/10.5194/amt-2019-230
Preprint. Discussion started: 5 July 2019

Atmospheric Measurement Techniques Discussions

Title: Nocturnal aerosol optical depth measurements with modified skyradiometer POM-02 using the moon as a light source

Authors:
Akihiro Uchiyama[1], Masataka Shiobara[2], Hiroshi Kobayashi[3], Tsuneo Matsunaga[1], Akihiro Yamazaki[4], Kazunori Inei[5], Kazuhiro Kawai[5], and Yoshiaki Watanabe[5]

[1]Center for Global Environmental Research, National Institute for Environmental Studies, Tsukuba, Ibaraki 305-8506, Japan
[2]National Institute of Polar Research, Midoricho, Tachikawa, Tokyo 190-8518, Japan
[3]University of Yamanashi, Takeda, Kofu, Yamanashi 400-8510, Japan
[4]Meteorological Research Institute, Japan Meteorological Agency, Tsukuba, Ibaraki 305-0052, Japan
[5]Prede Co., Ltd., Kamidaira, Fussa, Tokyo 197-0012, Japan

Correspondence to: Uchiyama Akihiro (uchiyama.akihiro@nies.go.jp)

Abstract

The majority of aerosol data are obtained from daytime measurements, and there are few datasets available for studying nighttime aerosol characteristics. In order to estimate the aerosol optical depth (AOD) and the precipitable water vapor (PWV) during the nighttime using the moon as a light source, a skyradiometer POM-02 (Prede Ltd., Japan) was modified. The amplifier was adjusted so that POM-02 could measure lower levels of input irradiance. In order to track the moon based on the calculated values, a simplified formula was incorporated into the firmware. A new position sensor with a four-quadrant detector to adjust tracking of the sun and the moon was also developed.

The calibration constant, which is the sensor output for the extra-terrestrial solar and lunar irradiance at the mean earth-sun distance, was determined by using the Langley method. The measurements for the Langley calibration were conducted at the NOAA/MLO in October and November 2017. By assuming that the relative variation of the reflectance of the Robotic Lunar Observatory (ROLO) irradiance model is correct, the calibration constant for the lunar direct irradiance was successfully determined using the Langley method. The ratio of the calibration constant for the moon to that for the sun was often greater than 1; the value of the

https://doi.org/10.5194/amt-2019-230
Preprint. Discussion started: 5 July 2019

Atmospheric Measurement Techniques Discussions

ratio was 0.95 to 1.18 in the visible near-infrared wavelength region. This means that the ROLO model often underestimates the reflectance. In addition, this ratio depended on the phase angle. In this study, this ratio was approximated by a quadratic expression of the phase angle. By using this approximation, the reflectance of the moon can be calculated to within an accuracy of 1% or less.

In order to validate the estimates of the AOD and PWV, continuous measurements with POM-02 were conducted at MRI/JMA from January 2018 to May 2018, and the AOD and PWV were estimated. The results were compared with the AOD and PWV obtained by independent methods. The AOD was compared with that estimated from NIES High Spectral Resolution Lidar measurements (wavelength: 532 nm), and the PWV was compared with the PWV obtained from a radiosonde and the Global Positioning System. As a result, the estimations of the AOD and the PWV using the moon as the light source were made with the same degree of precision and accuracy as the estimates using the sun as the light source.

1. Introduction

Atmospheric aerosols are an important constituent of the atmosphere. Aerosols change the radiation budget directly by absorbing and scattering solar radiation and indirectly through their role as cloud condensation nuclei (CCNs), thereby increasing cloud reflectivity and lifetime (e.g., Ramanathan et al. 2001; Lohmann and Feichter 2005). Aerosols also affect human health as one of the main components of air pollution (Dockery et al. 1993; WHO 2006, 2013).

Atmospheric aerosols have a large variability in time and space. Therefore, measurement networks covering an extensive area on the ground and from space have been developed and established to determine the spatiotemporal distribution of aerosols. Well-known ground-based networks include AERONT (AErosol RObotic NETwork) (Holben et al. 1998), SKYNET (Takamura et al. 2004), and PFR-GAW (Precision Filter Radiometer-Global Atmosphere Watch) (Wehrli 2005). These observation networks use passive radiometers which measure sunlight in the region from ultraviolet to shortwave infrared wavelengths and the column average effective aerosol characteristics such as aerosol optical depth (AOD) are retrieved.

Using lidar, which is an active remote sensing instrument, several networks have also been constructed: for example, the Micropulse Lidar Network (MPLNET) by NASA (National Aeronautics and Space Administration) (Welton et al. 2001; Levis et al. 2016), the European Aerosol Research Lidar Network (EARLINET) (Pappalardo

https://doi.org/10.5194/amt-2019-230
Preprint. Discussion started: 5 July 2019

Atmospheric Measurement Techniques Discussions

et al. 2016) in Europe, the Asian Dust and aerosol lidar observation network (AD-Net) (Shimizu et al. 2017) in east Asia, and the Latin American Lidar Network (LALINET) (Guerrero-Rascado et al. 2016) in South America.

Several satellite programs provide aerosol optical depth data on a global scale: for example, the Moderate Resolution Imaging Spectroradiometer (Remer et al. 2005), Multiangle Imaging Spectroradiometer (Kahn et al. 2005), Geostationary Operational Environmental Satellite (GOES) Aerosol Smoke Product (Prados et al. 2007), Sea-viewing Wide Field-of-view Sensor (Wang et al. 2000), Advanced Himawari Imager (AHI) (Yoshida et al. 2018; Kikuchi et al. 2018), and Cloud-Aerosol Lidar and Infrared Pathfinder Satellite Observation (CALIPSO; Winker et al. 2007).

With the exception of active sensor measurements such as lidar systems, to estimate aerosol characteristics, direct solar irradiance and scattered solar radiance measured with a passive sensor are required. Therefore, the majority of aerosol property data are obtained by daytime measurements, and there are few datasets of nighttime aerosol characteristics available.

To advance the understanding of the diurnal behavior of aerosols, and nocturnal mixing layer dynamics, nighttime continuous AOD measurements are necessary. In particular, in high latitude regions during the winter polar night, aerosol properties cannot be measured using sunlight, and this results in gaps in the long-term aerosol data. Such nocturnal aerosol data would also contribute to the understanding of aerosol transport to polar regions, the influence of aerosol on cloud formation, and the cloud effect on the radiation budget.

Lidar instruments can be used to obtain aerosol data during the night. However, in many cases, a value for the ratio of the extinction coefficient to the backscattering coefficient is often assumed in analysis using lidar, and in order to improve the accuracy of the analysis, constraining of the AOD is necessary.

In order to measure the optical depth of aerosol at night, research has been conducted using the moon and stars as light sources (Herber et al. 2002; Esposito et al. 1998; Esposito et al. 2003; Pérez-Ramírez et al. 2008). Since the reflectivity of the moon changes depending on the observation angle, the determination of the calibration coefficient is an important obstacle to overcome (Herber et al. 2002). Instruments for observing stars are large, expensive, and complicated to use due to the low level of incoming energy from stars. Therefore, stellar measurements are limited in use, and no large-scale observation network has been established.

The moon is a bright light source at night and the reflectance properties of the moon's surface are virtually invariant ($<10^{-8}\,\mathrm{yr}^{-1}$; Kieffer 1997). However, since the surface of the moon is not spatially uniform and has non-Lambertian reflectance, the

https://doi.org/10.5194/amt-2019-230
Preprint. Discussion started: 5 July 2019

Atmospheric Measurement Techniques Discussions

brightness of the moon as seen by an observer on the earth varies depending on the relationship between the moon, the sun, and the observer, that is, the phase and the lunar libration. Therefore, it is difficult to use the moon as a light source.

However, in the 2000s, the quality of reflectance data for the moon has improved. The empirical model known as ROLO (Robotic Lunar Observatory) was developed by the United States Geological Survey (USGS) (Kieffer and Stone 2005). ROLO is a NASA-funded program aimed at using the moon for on-orbit calibration of Earth Observing System (EOS) satellite instruments. Furthermore, the Spectral Profiler (SP) onboard the Japanese Selenological and Engineering Explorer (SELENE, nicknamed Kaguya) measures lunar photometric properties in the region of visible, near-infrared, and shortwave infrared wavelengths (Yokota et al. 2011). These data made it possible to estimate the reflectance of the moon, and thus the moon can be used as a light source for aerosol optical depth estimation.

The Cimel sun photometer used in AERONET has been modified for lunar observation and the aerosol optical depth at night can be estimated (Berkoff et al. 2011; Barreto et al. 2013, 2016, 2017).

In SKYNET, the radiometers POM-01 and POM-02, manufactured by Prede Co. Ltd., Japan, are used. These radiometers are called 'sky radiometers', and measure both the solar direct irradiance and sky-radiances (Takamura et al. 2004). The sky radiometers POM-01 and POM-02 (Prede Co. Ltd., Japan) can measure solar direct irradiance and sky-radiances during the daytime and the measured data are used for estimating aerosol characteristics during the daytime (Takamura et al. 2004). In this study, we will aim to measure the optical depth of aerosol using the moon as a light source by modifying POM-02.

In section 2, we describe our modification of the instrument. In section 3, the ROLO model is briefly explained. In section 4, we briefly describe the data used in this study. In section 5, the calibration method and corresponding results are described. In section 6, we show the results of comparing the aerosol optical thickness and precipitable water vapor obtained by continuous observation with those obtained by other independent instruments.

2. Modification of instrument

2.1 Adjustment of Amplifier

The skyradiometer POM-02 is designed to measure the direct solar irradiance and the scattered sky radiance with a single radiometer. An example of the calibration constant, which is the sensor output for the extra-terrestrial solar irradiance at the

https://doi.org/10.5194/amt-2019-230
Preprint. Discussion started: 5 July 2019

mean earth-sun distance (1 astronomical unit (AU)) at the reference temperature, is shown in Table 1. It is 1.8×10^{-5} to 3.4×10^{-4} A in the visible and near-infrared regions, and 7.9×10^{-5} to 1.3×10^{-4} A in the short-wavelength infrared region. Figure 1 shows an example of measurements of scattered radiances in the visible and near-infrared wavelength region. The output for the scattered radiance from the sky is 1×10^{-7} to 1×10^{-10} A, and this value is 1×10^{-6} smaller than the direct solar irradiance. The direct lunar irradiance is 1×10^{-5} as strong as the direct solar irradiance during a full moon, and 1×10^{-6} during a half-moon (Berkoff et al. 2011). The direct lunar irradiance during the half moon is about $2\times10^{-5}\times10^{-6}= 2\times10^{-11}$ in the 340 and 380 nm channels. This is nearly detectable limits of the current POM-02. Without the modification, it is possible to measure the direct lunar irradiance with the current POM-02 except for wavelengths between 340 and 380 nm where the sensitivity of the detector is low and wavelengths of 1225, 1627, and 2200 nm with poor S/N.

Table 2 shows the measurement range before and after modification of POM-02. POM-02 measures input energy in seven ranges according to the magnitude of the input energy, and the measured value is digitized with 15 bits. The measurement range was expanded slightly. The measurement limit depends on the magnitude of the dark current and the magnitude of the noise.

The dark current of the detector in the visible and near-infrared region was about 5×10^{-13} A, and the RMS of the random component of the noise was 4×10^{-14} A. In consideration of these values, the new POM-02 can use the amplifiers from range 1 to 7 and the minimum meaningful current is about 4×10^{-13} A (~RMS×10) in the visible and near-infrared region. This is 1×10^{-8} to 1×10^{-9} of the direct solar irradiance.

The dark current of the detector in the shortwave infrared wavelength region was about 1.5×10^{-8} A, and the RMS of the random component of the noise was 4×10^{-11} A. The new POM-02 can use the amplifiers from range 1 to 5 and the minimum meaningful current is about 4×10^{-10} A (~RMS×10). This value and the magnitude of the measured value of the direct lunar irradiance are comparable. It is difficult to measure direct lunar irradiance even with the new POM-02 in the shortwave infrared wavelength region.

2.2 Sun and moon position sensor

A position sensor with a four-quadrant detector is used to adjust the tracking of the sun and the moon. In order to adjust the tracking of the moon, a position sensor incorporating a new electronic circuit to amplify the signal and new software to

https://doi.org/10.5194/amt-2019-230
Preprint. Discussion started: 5 July 2019

process the signal data was developed. The new position sensor can be used to track both the sun and the moon. The function of the moon tracking adjustment works for a period of the full moon ± about 90 degrees of the phase angle (half-moon). The threshold value to operate the tracking adjustment can be specified by the user. For phase angles larger than the half-moon, the signal of the position sensor was small, and the position sensor was not used. When the POM-02 is accurately installed horizontally and directionally, it is possible to track the moon based on the calculated position values, and the direct irradiance of the moon could be measured during the full moon to within ± about 10 days, depending on the aerosol optical depth on the measurement day.

2.3 Simplified calculation of moon position

The moon positions were calculated with simplified formula in Nagasawa (1981). When comparing the moon position calculated by this simplified formula with that calculated using the NASA SPICE toolkit (Acton 1996), the difference in the zenith angle is less than 0.01 degrees, and the difference in the azimuth angle is less than 0.04 degrees. Therefore, if POM-02 is accurately installed horizontally and directionally, it is possible to track the moon with sufficient accuracy based on values calculated with the simplified formula.

3. Robotic Lunar Observatory (ROLO) irradiance model

In order to estimate the aerosol optical thickness using the moon as a light source, measurement of the extra-terrestrial irradiance of the moon is necessary. In this study, a model known as the ROLO irradiance model (Kieffer and Stone 2005) was used. This model was developed at the U.S. Geological Survey (USGS) and is based on an extensive database of radiance images acquired by the ground-based ROLO over more than 8 years. ROLO is a NASA-funded program designed to use the moon for on-orbit calibration of Earth Observing System (EOS) satellite instruments. The empirical irradiance model was developed for 32 wavelengths from 350 to 2450 nm and has the same form for each wavelength. The average residual is less than 1%. The coefficients of the empirical formula were constrained and determined using data with a phase angle between 1.55 and 97 degrees.

https://doi.org/10.5194/amt-2019-230
Preprint. Discussion started: 5 July 2019

Atmospheric Measurement Techniques Discussions

$$\ln A_k = \sum_{i=0}^{3} a_{ik} g^i + \sum_{j=1}^{3} b_{jk} \Phi^{2j-1} + c_1\phi + c_2\theta + c_3\Phi\phi + c_4\Phi\theta + d_{1k} e^{-g/p_1} + d_{2k} e^{-g/p_2} + d_{3k} \cos((g - p_3)/p_4) \quad (1)$$

where A_k is the disk-equivalent reflectance, g is the absolute phase angle in radians, θ and ϕ are the selenographic latitude and longitude of the observer in degrees, and Φ is the selenographic longitude of the sun in radians.

This formula must be used with caution. The equation in Kieffer and Stone (2005) has well-known typographical errors. In eq. (1), θ and ϕ in the original expression by Kieffer and Stone (2005) are exchanged. In addition, the units of the coefficients p_1, p_2, p_3, and p_4 are degrees. Therefore, in order to make the dimensions the same, g in the exponent and the cosine terms must be converted into units in degrees.

The astronomical parameter was calculated using our own software developed using the NASA SPICE toolkit; an observation geometry information system named SPICE is offered by NASA's Navigation and Ancillary Information Facility (NAIF) (Acton, 1996). SPICE is widely used in the NASA and international planetary exploration communities (for more information about SPICE, refer to the NAIF web page at http://naif.jpl.nasa.gov.).

In this study, only the values of the reflectance are used, and it is assumed that the relative changes in reflectance are correct. The reflectance values are not converted to irradiance values by assuming the extra-terrestrial solar spectral irradiance. The wavelength of POM-02 used in this study does not necessarily match the wavelength of the ROLO model. Here, the reflectance at the wavelength of POM-02 was calculated by linearly interpolating from the reflectance of the ROLO model at two adjacent wavelengths. In addition, the ROLO model does not have reflectance data for the wavelength 340 nm. The reflectance at the wavelength 340 nm was obtained by extrapolating linearly from the values at the two end wavelengths.

4. Data

4.1 Data for Langley calibration

The aerosol optical thickness is estimated by measuring the attenuation of the direct solar or lunar irradiance. Therefore, in order to estimate the aerosol optical thickness, the output of the instrument for the input irradiance at the top of the

https://doi.org/10.5194/amt-2019-230
Preprint. Discussion started: 5 July 2019

atmosphere is necessary. The determination of this constant is referred to as calibration, and the output of the instrument for the extra-terrestrial solar or lunar irradiance at the mean earth-sun distance (1 AU) at the reference temperature is called the calibration constant. In this study, the calibration constant was determined by the Langley method.

To calibrate the POM-02 by the Langley method, measurements were conducted at the NOAA Mauna Loa Observatory (MLO) during the period from Sep. 28, 2017 to Nov. 7, 2017; the full moon was on Oct. 4 and Nov. 3, 2017. The MLO (19.5362°N, 155.5763°W) is located at an elevation of 3397.0 meters amsl on the northern slope of Mauna Loa, Island of Hawaii, Hawaii, USA. The atmospheric pressure is about 680 hPa. The MLO is one of the most suitable places to obtain data for a Langley plot for the solar direct irradiance measurement (Shaw 1983). Though the air at MLO is highly transparent, it is affected in the late morning and afternoon hours by marine aerosol that reaches the observatory during the marine inversion boundary layer breakdown under solar heating (Shaw 1983; Perry et al. 1999). Therefore, using data taken in the morning is recommended (Shaw 1982; Dutton et al. 1994; Holben et al. 1998).

However, during the nighttime, the upslope winds change to downslope winds, which bring low moisture and aerosol-poor air above the marine boundary layer down to the observatory. As a result, daytime orographic clouds at the observatory disappear and the atmosphere stratification becomes stable. These atmospheric conditions are suitable for obtaining data for the Langley plot from the lunar direct irradiance measurement.

4.2 Continuous measurement for comparison

The measurements for the estimation of the aerosol optical depth and precipitable water vapor were performed at 1-minute intervals at the Japan Meteorological Agency/Meteorological Research Institute (JMA/MRI) (36.05°N, 140.13°E) in Tsukuba, which is located about 50 km northeast of Tokyo. The comparison was made using data obtained during the period from Jan. 1 to May 31, 2018. During this period, the AOD and the precipitable water vapor (PWV) were estimated assuming the calibration constant was unchanged.

The optical depth estimated from POM-02 was compared with the value of the NIES High Spectral Resolution Lidar (HSRL, wavelength; 532 nm). The NIES/HSRL is one of the lidar operated by the lidar measurement group of the National Institute for Environmental Studies (NIES) (Shimizu et al. 2016). The NIES and MRI

https://doi.org/10.5194/amt-2019-230
Preprint. Discussion started: 5 July 2019

Atmospheric Measurement Techniques Discussions

observation sites are located about 800 m apart. Since the POM-02 was not measured at the 532 nm wavelength, the AOD at 532 nm was interpolated from the values of 500 nm and 675 nm by assuming that AOD is proportional to $\lambda^{-\alpha}$, where λ is the wavelength. Furthermore, since the AOD of NIES/HSRL is the 15-minute average, the value of POM-02 was also averaged over 15 minutes.

The PWV estimated from POM-02 was compared with that obtained from the vertical profile of a radiosonde and that obtained from the Global Positioning System (GPS) receiver. The radiosonde observation is operated from the JMA Aerological Observatory, which is adjacent to JMA/MRI. The GPS receiver is installed at JMA/MRI, and GPS data were processed by one of the JMA/MRI researchers (Shoji et al. 2013). The comparison of the PWV was performed using the 30-minute average values.

5. Calibration of POM-02 using MLO data

5.1 Method

The AOD and PWV are estimated by measuring the attenuation of the direct solar or lunar irradiances. Therefore, it is necessary to know the output of the instrument for extra-terrestrial solar or lunar irradiances. This output at the mean earth-sun distance (1 AU) at the reference temperature is called the calibration constant. In this study, the calibration constant was determined by the Langley method (Uchiyama et al. 2018). Here, we do not consider the temperature dependence of the sensor output for the POM-02. Under these observation conditions in Tsukuba, the temperature dependence of the sensor output can be ignored except for the 340, 380, and 2200 nm channels (Uchiyama et al. 2018).

The sensor output when measuring the direct solar irradiance can be written as follows:

$$V(\lambda_0) = \frac{V_{S0}(\lambda_0)}{R_S{}^2} \exp(-m(\theta)\tau(\lambda_0)) \overline{T}_{gas}(\lambda_0, \theta) \tag{2}$$

where $V(\lambda_0)$ is the sensor output in the λ_0 wavelength channel, R_S is the earth-sun distance in AU, $m(\theta)$ is the total airmass, $\tau(\lambda)$ is the total optical depth, θ is the solar zenith angle, and $\overline{T}_{gas}(\lambda_0, \theta)$ is the channel average transmittance of the gas line absorption. Furthermore, $V_{S0}(\lambda_0)$ is the sensor output for the extra-terrestrial solar irradiance at 1 AU, and is called the calibration

https://doi.org/10.5194/amt-2019-230
Preprint. Discussion started: 5 July 2019

constant. $\tau(\lambda)$ consists of the optical thickness for molecular scattering (Rayleigh scattering), aerosol, and the continuous absorption of gas. In this study, it is assumed that airmass $m(\theta)$ is the same for all components. The airmass $m(\theta)$ for molecular scattering is often used (Schmid and Wehrli 1995; Holben et al. 1998).

In the case of no "gas absorption", the following equation is used:

$$V(\lambda_0) = \frac{V_{S0}(\lambda_0)}{{R_S}^2} \exp(-m(\theta)\tau(\lambda_0)) \tag{3}$$

Taking the logarithm of the equation leads to

$$\begin{aligned} \ln(V(\lambda_0){R_S}^2) &= \ln V_{S0}(\lambda_0) - m(\theta)\tau(\lambda_0) \\ &= C_1 m(\theta) + C_2 \end{aligned} \tag{4}$$

The parameters on the left-hand side are known: V is the measurement value, and R_S and $m(\theta)$ can be calculated from the solar zenith angle. For example, R_S can be calculated with the simplified formula in Nagasawa (1981), and $m(\theta)$ can be calculated as in Kasten and Young (1989). In the case of POM-02, the sensor output is the current, and the unit of the measurements of V is the ampere A. $C_2 = \ln V_{S0}$ is determined from the ordinate intercept of a least-square fit when one plots the left-hand side of the above equation versus airmass $m(\theta)$.

For the water vapor absorption band at a wavelength of 940 nm, the Beer-Lambert-Bouguer law is not valid. Calibration methods for the 940 nm channel, which is in the water vapor absorption band, have been considered extensively in previous studies (Reagan et al. 1987a, 1987b, 1995; Bruegge et al. 1992; Thome et al. 1992, 1994; Michalsky et al. 1995, 2001; Schmid et al. 1996, 2001; Shiobara et al. 1996; Halthore et al. 1997; Cachorro et al. 1998; Plana-Fattori et al. 1998, 2004; Ingold et al. 2000; Kiedron et al. 2001, 2003; Uchiyama et al. 2014, Campanelli et al. 2014).

In this study, the modified Langley method is used (Reagan et al. 1987a; Bruegge et al. 1992; Schmid and Wehrli 1995). In the modified Langley method, the transmittance is approximated by an empirical formula. The water vapor transmittance is approximated as follows:

$$Tr(\mathrm{H2O}) = \exp(-a(m(\theta)\cdot pwv)^b) \tag{5}$$

where a and b are fitting coefficients, and pwv is PWV.

Coefficients a and b were determined by computing the transmittance for several atmospheric models (Uchiyama et al. 2014).

https://doi.org/10.5194/amt-2019-230
Preprint. Discussion started: 5 July 2019

Atmospheric Measurement Techniques Discussions

The output of the 940 nm channel can be written as follows;

$$
\begin{aligned}
V(\lambda_0) &= \frac{V_{S0}(\lambda_0)}{{R_S}^2}\exp(-m(\theta)\tau(\lambda_0))Tr(\mathrm{H2O}) \\
&= \frac{V_{S0}(\lambda_0)}{{R_S}^2}\exp(-m(\theta)\tau(\lambda_0))\exp(-a(m(\theta)\cdot pwv)^b)
\end{aligned}
\tag{6}
$$

Taking the logarithm of the equation leads to

$$
\begin{aligned}
\ln V{R_s}^2 + m(\theta)(\tau_{aer} + \tau_R) &= \ln V_{S0} - a(pwv)^b m(\theta)^b \\
&= C_1 m(\theta)^b + C_2
\end{aligned}
\tag{7}
$$

In the same way as the normal Langley method, the parameters on the left-hand side are known: V is the measurement value, and R and $m(\theta)$ can be calculated from the solar zenith angle. τ_R is also estimated from the surface pressure; for example, τ_R can be calculated as in Asano et al. (1983). In addition, τ_{aer} is the aerosol optical depth at the 940 nm wavelength, which is interpolated from the aerosol optical depth from the values at the 870 and 1020 nm wavelengths.

If pwv is constant, then the right-hand side of the equation is a linear function of $m(\theta)^b$. Therefore, the values on the left-hand side can be fitted by a linear function of $m(\theta)^b$, and the intersection of the y-axis and the fitted line is $\ln V_{S0}$.

The sensor output when measuring the direct lunar irradiance can be written as follows:

$$
V(\lambda_0) = \frac{A_{ROLO}}{\pi}\Omega_M \frac{V_{S0}(\lambda_0)}{{R_S}^2}\cdot\frac{1}{{R_m}^2}\exp(-m(\theta)\tau(\lambda_0))\overline{T}_{gas}(\lambda_0,\theta)
\tag{8}
$$

where A_{ROLO} is the lunar reflectance by the ROLO irradiance model, Ω_M is the solid angle of the moon, R_S is the distance between the moon and the sun in AU, and R_m is the distance between the moon and the observer in AU.

It is assumed that the relative variation of the reflection of the ROLO model is correct. This assumption means that the reflectance of the moon is assumed to be $C \cdot A_{ROLO}$, where C is a constant. A_{ROLO} in eq. (8) is replaced with $C \cdot A_{ROLO}$.

https://doi.org/10.5194/amt-2019-230
Preprint. Discussion started: 5 July 2019

Atmospheric Measurement Techniques Discussions

$$V(\lambda_0) = \frac{C \cdot A_{ROLO}}{\pi} \Omega_M \frac{V_{S0}(\lambda_0)}{{R_S}^2} \cdot \frac{1}{{R_m}^2} \exp(-m(\theta)\tau(\lambda_0)) \overline{T}_{gas}(\lambda_0, \theta) \quad (9)$$

In the case of no "gas absorption", taking the logarithm of the equation leads to

$$\begin{aligned} \ln\left(\frac{\pi V(\lambda_0)}{A_{ROLO}\Omega_M} {R_S}^2 {R_m}^2\right) &= \ln C V_{S0}(\lambda_0) - m(\theta)\tau(\lambda_0) \\ &= \ln V_{m0}(\lambda_0) - m(\theta)\tau(\lambda_0) \\ &= C_1 m(\theta) + C_2 \end{aligned} \quad (10)$$

where $V_{m0}(\lambda_0) = C V_{S0}(\lambda_0)$. $C_2 = \ln V_{m0}$ is determined from the ordinate intercept of a least-square fit when one plots the left-hand side of the above equation versus airmass $m(\theta)$.

V_{S0} can be determined by applying the Langley method to data taken during the daytime. If V_{S0} is determined, the coefficient C can be determined by taking the ratio of V_{m0} and V_{S0}. If the coefficient C is 1, the reflectance of the ROLO model will be correct. If the coefficient C is greater than 1 (less than 1), the reflectance in the ROLO model is under-estimated (over-estimated).

5.2 Results

Examples of Langley plots in the visible and near-infrared wavelengths are shown in Fig. 2. In these examples, the regression lines can be well determined for any wavelength. $C_2 = \ln V_{m0}$ is determined from the ordinate intercept of the regression line (see eq. (10)). At the 340 nm wavelength, the regression line tends to deviate from the measured values in the region of airmasses larger than 6. It is presumed that the detector output at the 340 nm wavelength is small and hence the detector output may be nonlinear. The output at that time is about 1×10^{-12} A. When using output values less than this, the user needs to treat there results with caution. At the 940 nm wavelength, the modified Langley method was applied. In this example, the regression line equation provides a good fit.

In Fig. 3, examples of the Langley plot in the shortwave infrared region (1225, 1627, 2200 nm) are shown. The detector output of these channels are from 2×10^{-10} to

https://doi.org/10.5194/amt-2019-230
Preprint. Discussion started: 5 July 2019

5×10^{-10} A, and the root mean square error of the random noise is 4×10^{-11} A. The ratio of noise to detector output is large and it is difficult to use these channels for estimating the aerosol optical depth.

In Fig. 4, the relationship between the coefficient $C(=V_{m0}/V_{S0})$ and the phase angle in the visible and near-infrared wavelength region (from 340 to 1020 nm) is shown. As shown in the previous section, the coefficient C is the ratio of the calibration constant for the moon and sun, which indicates the error of the ROLO irradiance model reflectance and thus the ROLO irradiance model reflectance can be corrected using the coefficient C. As can be seen from this figure, the coefficient C is often greater than 1 and depends on the phase angle. At most wavelengths, the coefficient C is small when the absolute value of the phase angle is small (near the full moon) and increases as the absolute value of the phase angle increases. The range of C is 0.95 to 1.18. The absorption band of water vapor is at the 940 nm wavelength, and the accuracy of both V_{S0} and V_{m0} is poor. Therefore, no clear relationship between C and the phase angle is found, but the coefficient C is about 1.16. The fact that C is larger than 1 means that the reflectance of the ROLO irradiance model is underestimated.

In Fig. 5, the relationship between the coefficient $C(=V_{m0}/V_{S0})$ and the phase angle in the shortwave infrared wavelength region (1225, 1627, 2200 nm) is shown. In these channels, the error of C is large, but the coefficient C depends on the phase angle as in the visible and near-infrared wavelength region; C is small when the phase angle is near zero and increases as the absolute value of the phase angle increases.

In this study, the phase angle dependence of the coefficient C is approximated by a quadratic equation of the absolute value of the phase angle:

$$C = A_c \cdot g^2 + B_c \quad (11)$$

where g is the phase angle.

That is,

$$V_{m0} = V_{S0} \cdot (A_c \cdot g^2 + B_c) \quad (12)$$

The coefficients, A_c and B_c are shown in Table 3. The regression line was plotted in Figs. 4 and 5. By using this approximation, the reflectance of the ROLO model can

https://doi.org/10.5194/amt-2019-230
Preprint. Discussion started: 5 July 2019

be estimated to within 1% in most channels. By using this approximation, the data processing to estimate the aerosol optical depth from the measured value becomes straightforward.

The error of the reflectance in the ROLO irradiance model is dependent on the phase angle. Here, although it was approximated by the second-order regression equation, there still remains error beyond the uncertainty of the Langley plot. These errors may be caused by the effect of the libration. It is necessary to further accumulate the reflectance data of the moon.

6. Examples of measurement

In order to validate the estimations of AOD and PWV, we compared them with the AOD and PWV obtained by independent methods.

6.1 Aerosol optical depth (AOD)

The AOD estimated from POM-02 was compared with the value of the NIES/HSRL (wavelength: 532 nm). The AOD at 532 nm was interpolated from the values for 500 and 675 nm by assuming that the AOD is proportional to $\lambda^{-\alpha}$, where λ is wavelength.

Figures 6 (a) and (b) show the scatter plot of the aerosol optical depth during the daytime and nighttime, respectively. In Fig. 6 (c), the scatter plot during the nighttime is shown together with that during the daytime. Table 4 shows the results of the comparison between NIES/HSRL and POM-02 AOD: the statistics of the difference between the two AODs, the coefficients of the linear regression equation of NIES/HSRL and POM-02 AOD ($\tau_{HSRL} = C_1 \cdot \tau_{POM\,02} + C_2$.), the RMSE of the residual, the 95% confidence interval of the coefficients, and the number of observations.

The difference in the slope value of the regression coefficients is 0.1600 (= 1.0477 − 0.8877). The 95% confidence interval of the coefficient is about ±0.04 during both the daytime and the nighttime. It cannot be said that the slopes of the two regression lines are equal based on their 95% confidence intervals. However, the correlation between NIES/HSRL and POM-02 AOD is high, and the difference between them and their RMSEs are similar. Furthermore, as shown in Fig. 6 (c), the scatter diagrams for the daytime and nighttime are almost overlapping, and it seems that the two sets of measurements obtain similar results.

Examples of time series of the AOD from NIES/HSRL and POM-02 are shown in

https://doi.org/10.5194/amt-2019-230
Preprint. Discussion started: 5 July 2019

Fig. 7. As can be seen from these figures, the AOD of the daytime and nighttime estimated from POM-02 constitute a continuous series. The AOD from NIES/HSRL and that from POM-02 have similar time variations. However, while there are periods when the values are consistent, there are periods when there are systematic differences.

In NIES/HSRL data processing, the AOD below an altitude of 500 m is calculated by using the value of the extinction coefficient for an altitude of 500 m. Since the height of the atmospheric boundary layer is typically 1500 to 2000 m, a large amount of aerosols exist at altitudes below 500 m. If the actual distribution deviates from the assumed distribution, the estimated AOD is shifted systematically.

6.2 Precipitable water vapor (PWV)

The PWV estimated from POM-02 was compared with that obtained from the vertical profile of the radiosonde and that obtained from the GPS receiver. The PWV estimated from the radiosonde data has a frequency of two values per day, whereas the PWV obtained from GPS is continuous.

6.2.1 Radiosonde

The PWV from a radiosonde is often used as a reference for the PWV measurement value. The PWV from the radiosonde and PWV from POM-02 are first compared. Figure 8 shows a scatter plot of the PWV from the radiosonde and from POM-02. The red symbol denotes 00 UTC (09 LTC), and the blue symbol is 12 UCT (21 LTC). Table 5 shows the results of the comparison between the radiosonde and POM-02 precipitable water vapor: statistics of the difference between both PWV, the coefficients of the linear regression equation of the radiosonde and POM-02 PWV ($PWV_{POM-02} = C_1 \cdot PWV_{Sonde} + C_2$), the RMSE of residual, 95% confidence interval of the coefficients, and number of data. The ratio of PWV estimated from POM-02 and the radiosonde in both daytime and nighttime is almost constant: the slope of the regression line is 0.80 in the daytime and 0.78 in the nighttime.

The empirical formula of the transmittance is expressed as eq. (5). The ratio of the two PWVs is almost constant. In addition, as shown in Fig. 4, the modified Langley plot provides a good fit for the data. From these facts, it seems that the value of the coefficient b of eq. (5) is appropriate but the value of the coefficient a of eq. (5) was inappropriate. It is possible that the filter characteristics of the 940 nm channel

https://doi.org/10.5194/amt-2019-230
Preprint. Discussion started: 5 July 2019

have changed from the nominal characteristics due to degradation.

Let $pwv = c \cdot pwv'$ and rewrite eq. (5) as follows:

$$\begin{aligned} Tr(\mathrm{H2O}) &= \exp(-a(m(\theta)\cdot(c\cdot pwv'))^{b}) \\ &= \exp(-ac^{b}(m(\theta)\cdot pwv')^{b}) \end{aligned} \tag{13}$$

Then the PWV can be corrected by replacing a with ac^{b}.

Figure 9 shows a scatter plot of the PWV from the radiosonde and the corrected PWV from POM-02. For the correction coefficient c, the average value of the coefficients C_1 of the daytime and nighttime regression equations was used. Table 6 shows the results of the comparison between the radiosonde and corrected POM-02 precipitable water vapor: the statistics of the difference between both PWV, the coefficients of the linear regression equation $PWV_{POM-02}(\mathrm{corrected}) = C_1 \cdot PWV_{Sonde} + C_2$, the RMSE of the residual, the 95% confidence interval of coefficients, and the number of observations.

The slope C_1 of the regression line during the daytime and nighttime is 1.0160 and 0.9869, respectively, and the difference between them is 0.0291 (= 1.0160 − 0.9869). The 95% confidence intervals of the slopes during the daytime and nighttime are ± 0.0206 and ± 0.0271, respectively. The difference between them is 0.0291, which is larger than the respective 95% confidence intervals. Therefore, the two slopes are not equivalent based on the 95% confidence intervals.

However, since the slope of the regression line determined using all of the data is 1.0042 and the 95% confidence interval is ±0.0173, the three slopes of the regression lines can be regarded as equivalent at the 95% confidence level. Furthermore, there are no large differences in the bias, RMSE, and correlation coefficient between PWV from the radiosonde and POM-02. Therefore, the PWVs of daytime and nighttime for POM-02 are presumed to have the same degree of precision and accuracy.

6.2.2 GPS

Next, the result of the comparison between the PWV obtained from POM-02 and GPS is shown. Before that, the result of the comparison between the PWV obtained from GPS and the radiosonde is shown in Fig. 10. Table 7 shows the results of the comparison between GPS and radiosonde precipitable water vapor: the statistics of the difference between both PWV, the coefficients of the linear regression equation

https://doi.org/10.5194/amt-2019-230
Preprint. Discussion started: 5 July 2019

$PWV_{Sonde} = C_1 \cdot PWV_{GPS} + C_2$, the RMSE of the residual, the 95% confidence interval of the coefficients, and the number of observations.

The slope of the regression line in Fig. 10 is about 0.94. In the region of the PWV less than 2 g/cm^2, the PWV from GPS tends to be smaller than the PWV from the radiosonde. In the region of PWV more than 3 g/cm^2, the difference between PWV from GPS and the radiosonde is more scattered. Therefore, the slope of the regression line became smaller than 1. In a previous comparison conducted by the authors, the slope of the regression line was almost 1 (Uchiyama et al. 2014). There is a possibility that the PWV from GPS used in this study has a larger error than the PWV used previously.

Figure 11 shows a scatter diagram of the PWV from GPS and the corrected PWV from POM-02. Table 8 shows the results of the comparison between PWV from GPS and corrected PWV from POM-02: statistics of difference between the two PWVs, the coefficients of the linear regression equation, the RMSE of the residuals, the 95% confidence interval of the coefficients, and the number of observations.

The slope of the regression line is about 0.91 for both the daytime and nighttime. Similar to the results of the comparison between the PWV from the radiosonde and GPS, in the region of PWV from GPS less than 2 g/cm^2, the PWV from GPS tends to be somewhat smaller than the PWV from POM-02 during both the daytime and nighttime. In the region of PWV greater than 3 g/cm^2, the difference between PWV from GPS and the radiosonde is more scattered.

The difference between the slopes of the regression lines is 0.0076 (= 0.9132 − 0.9056) and the 95% confidence intervals during the daytime and nighttime are ±0.0097 and ±0.0221, respectively. Therefore, the confidence intervals of the two slopes are overlapping, and the values of slopes can be regarded as equivalent at the 95% confidence level.

In Fig. 11 (c), the scatter plot obtained using nighttime data is shown together with that obtained using daytime data. The data obtained during the daytime and nighttime overlap, and it seems that the PWV from POM-02 during the daytime and nighttime are estimated with the same degree of precision and accuracy.

Examples of time series of PWV from GPS and POM-02 are shown in Fig. 12. The PWV from GPS and that from POM-02 have similar time variations. Although there are some systematic differences in Fig. 12 (b), the PWV from GPS and the PWV from POM-02 almost overlap in Figs. 12 (a) and (c). In addition, the PWV during the daytime and nighttime estimated from POM-02 are continuously connected.

https://doi.org/10.5194/amt-2019-230
Preprint. Discussion started: 5 July 2019

7. Summary and conclusion

Aerosol data are often estimated using the solar direct irradiance and the solar scattered radiance. Therefore, the majority of data on aerosol properties are obtained using daytime measurements, and there are few data available on aerosol characteristics at night. In order to estimate the aerosol optical depth (AOD) and the precipitable water vapor (PWV) during the nighttime using the moon as a light source, POM-02 (Prede Ltd., Japan), which is used to estimate aerosol characteristics during the daytime, was modified.

The current POM-02 has the ability to measure the direct irradiance from the moon for some channels in the visible and near-infrared wavelength region without the modification. Several modifications were made to measure the AOD during the nighttime and the measurement range was expanded slightly.

The amplifier was adjusted so that POM-02 could measure up to about 5×10^{-13} A: the lunar direct irradiance can be measured in the wavelength range of 340 to 1020 nm.

In order to track the moon based on the calculated value, the simplified formula by Nagasawa (1981) was incorporated into the firmware.

A position sensor with a four-quadrant detector is used to adjust the tracking of the sun and the moon. In order to adjust the tracking of the moon, a position sensor incorporating a new electronic circuit to amplify the signal and new software to process the signal data were developed. The new position sensor can be used to track both the sun and the moon.

The calibration constant was determined by using the Langley method. The measurements of the solar and lunar direct irradiance were conducted at the NOAA/MLO during the period from Sep. 28 to Nov. 7, 2017. Assuming that the relative variation of the reflectance of the ROLO irradiance model is correct, the calibration constant for the lunar direct irradiance was determined by using the Langley method. The calibration by the Langley method was successfully performed.

The ratio of the calibration constant for the moon to that for the sun was often greater than 1. This ratio shows the error of the ROLO irradiance model: the error of the moon reflectance. The value of the ratio was 0.95 to 1.18 in the visible near-infrared wavelength region. This means that the ROLO model often underestimates the reflectance. In addition, this ratio depended on the phase angle: when the phase angle was small (near the full moon), the ratio was small, and as the phase angle became larger, the ratio increased. In this study, this ratio was approximated by the quadratic expression of the phase angle. By using this

https://doi.org/10.5194/amt-2019-230
Preprint. Discussion started: 5 July 2019

approximation, the reflectance of the moon can be calculated to within an accuracy of 1% or less.

The continuous measurement of POM-02 was conducted at MRI/JMA from January 2018 to May 2018, and the AOD and PWV were estimated. In order to validate the estimates of the AOD and PWV, we compared them with the AOD and PWV obtained by independent methods. The AOD was compared with the AOD (532 nm) estimated from NIES/HSRL, and the PWV was compared with the PWV from the radiosonde and GPS.

Concerning the AOD, there were sometimes systematic differences between NIES/HSRL and POM-02. The cause of the systematic difference seems to be that NIES/HSRL assumes a constant extinction coefficient at altitudes of less than 500 m. The slopes of the linear regression lines during the daytime and nighttime could not be said to be equivalent at the 95% confidence level, but the scatter diagrams of the daytime and nighttime were almost overlapping. Therefore, the nighttime AOT was estimated with the same degree of precision and accuracy as the daytime AOT.

Concerning the PWV, the slopes of the linear regression lines during the daytime and nighttime were equivalent at the 95% confidence level in the comparisons between the PWV from POM-02 and the radiosonde and in the comparison between the PWV from POM-02 and GPS. Furthermore, the scatter diagrams of the daytime and the nighttime data were almost overlapping. Therefore, the PWV at nighttime can be estimated with the same degree of precision and accuracy as daytime PWV.

From these facts, the estimation of the AOD and the PWV using the moon as the light source has the same degree of precision and accuracy as the estimation using the sun as the light source.

In this study, the calibration was performed using about 40 days of data including two full moon days. As a result, it was found that there was an error in the reflectance of the ROLO irradiance model. In the future, it is necessary to accumulate more data for calibration and to reduce the error of the ROLO irradiance model. It is said that the ROLO model can be applied over a phase angle range of about 90 degrees. POM-02 has the ability to measure the direct lunar irradiance up to a phase angle range of about 120 degrees. It is necessary to expand the ROLO irradiance model so that it can be applied to larger phase angles.

It is now possible to estimate the aerosol optical depth during the nighttime. It is necessary to promote the adoption of this system in the existing observation network. After that, it is necessary to use the data obtained by using this instrument in the field of aerosol science at night, for the validation of aerosol transport models, and input data of the assimilation system.

https://doi.org/10.5194/amt-2019-230
Preprint. Discussion started: 5 July 2019

Data availability.

Data used in this study are available from the corresponding author.

Authors contributions.

This study was designed by AU, MS, HK and TM. The measurements of sky radiometer were conducted by AU, AK, KI and YW. The adjustment of amplifier and the development of position sensor were performed by MS, HK, KI, KK and YW. The development of the related software and the data analyses were performed by AU. The manuscript was written by AU, and all authors contributed to editing and revision.

Competing interests.

The authors declare that they have no conflict of interest.

Acknowledgements

This work was supported by the NIES GOSAT-2 project, Japan. This work was also supported by JSPS KAKENHI Grant Number 17K00531. We would like to thank Dr. Y. Jin and Dr. T. Nishizawa of NIES for providing NIES/HSRL data for comparison of the aerosol optical depth. We also would like to thank Dr. Y. Shoji of JMA/MRI for providing GPS data for the comparison of precipitable water vapor.

References

Acton Jr, C. H.: Ancillary data services of NASA's Navigation and Ancillary Information Facility, *Planet. Space Sci.*, **44**, Issue 1, 65-70, 1996.

Asano, S., Murai, K., and Yamauchi, T.: An improvement of the computation method of the atmospheric turbidity factors, *J. Meteorol. Res.*, **35**, 135-144, 1983 (in Japanese).

Barreto, A., Cuevas, E., Damiri, B., Guirado, C., Berkoff, T., Berjón, A. J., Hernández, Y., Almansa, F., and Gil, M.: A new method for nocturnal aerosol measurements with a lunar photometer prototype, *Atmos. Meas. Tech.*, **6**, 585–598, https://doi.org/10.5194/amt-6-585-2013, 2013.

Barreto, Á., Cuevas, E., Granados-Muñoz, M.-J., Alados- Arboledas, L., Romero, P. M., Gröbner, J., Kouremeti, N., Almansa, A. F., Stone, T., Toledano, C., Román, R., Sorokin, M., Holben, B., Canini, M., and Yela, M.: The new sun-skylunar Cimel CE318-T multiband photometer – a comprehensive performance evaluation, *Atmos. Meas. Tech.*, **9**, 631–654, https://doi.org/10.5194/amt-9-631-2016, 2016.

Barreto, Á., Román, R., Cuevas, E., Berjón, A. J., Almansa, A. F., Toledano, C.,

https://doi.org/10.5194/amt-2019-230
Preprint. Discussion started: 5 July 2019

Atmospheric Measurement Techniques Discussions

González, R., Hernández, Y., Blarel, L., Goloub, P., Guirado, C., and Yela, M.: Assessment of nocturnal aerosol optical depth from lunar photometry at the Izaña high mountain observatory, *Atmos. Meas. Tech.*, **10**, 3007–3019, https://doi.org/10.5194/amt-10-3007-2017, 2017.

Berkoff, T. A., Sorokin, M., Stone, T., Eck, T. F., Hoff, R., Welton, E., and Holben, B.: Nocturnal aerosol optical depth measurements with a small-aperture automated photometer using the moon as a light source, *J. Atmos. Ocean. Tech.*, 28, 1297–1306, https://doi.org/10.1175/JTECH-D-10-05036.1, 2011.

Bruegge, C. J., Conel, J. E., Green, R. O., Margolis, J. S., Holm, R. G., and Toon, G.: Water vapor column abundance retrievals during FIFE, *J. Geophys. Res.*, **97**, 18,759–18,768, 1992.

Cachorro, V. E., Utrillas, P., Vergaz, R., Duran, P., de Frutos, A. M., and Martinez-Lozano, J. A.: Determination of the atmospheric-water-vapor content in the 940-nm absorption band by use of moderate spectral-resolution measurements of direct solar irradiance. *Appl. Opt.*, **37**, 4678–4689, 1998.

Campanelli, M., Nakajima, T., Khatri, P., Takamura, T., Uchiyama, A., Estellés, V., Liberti, G. L., Malvestuto, V.: Retrieval of characteristic parameters for water vapour transmittance in the development of ground based Sun-Sky radiometric measurements of columnar water vapour, *Atmos. Meas. Tech.*, **7**, 1075–1087, doi:10.5194/amt-7-1075-2014, 2014.

Dockery, D. W., Pope, C. A., Xu, X., Spengler, J. D., Ware, J. H., Fay, M. E., Ferris, Jr., B. G., and Speizer, F. E.: An Association between Air Pollution and Mortality in Six U.S. Cities. *New Engl. J. Med.*, **329**, 1753-1759, 1993.

Dutton, E.G., Reddy, P., Ryan, S., and DeLuisi, J.: Features and Effects of Aerosol Optical Depth Observed at Mauna Loa, Hawaii: 1982-1992. *J. Geophys. Res.* **99**, 8295-8306, 1994.

Esposito, F., Serio, C., Pavese, G., Auriemma, G., and Satriano, C.: Measurements of nighttime atmospheric optical depth preliminary data from a mountain site in southern Italy. *J. Aerosol Sci.*, 29 (10), 1213–1218, 1998.

Esposito, F., Mari, S., Pavese, G., and Serio, C.: Diurnal and Nocturnal Measurements of Aerosol Optical Depth at a Desert Site in Namibia, *Aerosol Science and Technology*, **37**, 392-400, DOI: 10.1080/02786820300972, 2003.

Guerrero-Rascado, J. L., Landulfo, E., Antuña, J. C., Barbosa, H. de M. J., Barja, B., Bastidas, Á. E., Bedoya, A. E., da Costa, R. F., Estevan, R., Forno, R., Gouveia, D. A., Jiménez, C., Larroza E. G., da Silva Lopes, F. J., Montilla-Rosero, E., Moreira, G. de A., Nakaema, W. M., Nisperuza, D., Alegria, D., Múnera, M., Otero, L., Papandrea, S., Pallota, J. V., Pawelko, E. Quel, E. J., Ristori, P., Rodrigues, P. F.,

https://doi.org/10.5194/amt-2019-230
Preprint. Discussion started: 5 July 2019

Salvador, J., Sánchez, M. F., and Silva, A.: Latin American Lidar Network (LALINET) for aerosol research: diagnosis on network instrumentation, *J. Atmos. Sol. Terr. Phys.*, **138–139**, 112–120, 2016.

Halthore, R. N., Eck, T. F., Holben, B. N., and Markham, B. L.: Sun photometric measurements of atmospheric water vapor column abundance in the 940-nm band. *J. Geophys. Res.*, **102**(D4), 4343–4352, doi:10.1029/96JD03247, 1997.

Herber, A., Thomason, L. W., Gernandt, H., Leiterer, U., Nagel, D., Schulz, K-H., Kaptur, J., Albrecht, T., and Notholt, J.: Continuous day and night aerosol optical depth observations in the Arctic between 1991 and 1999. *J. Geophys. Res.*, 107, 4097, doi:10.1029/2001JD000536, 2002.

Holben, B. N., Eck, T. F., Slutsker, I., Tanré, D., Buis, J. P., Setzer, A., Vermote, E., Reagan, J. A., Kaufman, Y. J., Nakajima, T., Lavenu, F., Jankowiak, I., and Smirnov, A.: AERONET-A federated instrument network and data archive for aerosol characterization. *Remote Sens. Environ.*,**66**, 1-16, 1998.

Ingold, T., Schmid, B., Matzler, C., Demoulin, P., and Kampfer, N.: Modeled and empirical approaches for retrieving columnar water vapor from solar transmittance measurements in the 0.72, 0.82, and 0.94 μm absorption bands. *J. Geophys. Res.*, **105**, 24,327–24,343, 2000.

Kahn, R. A., Gaitley, B. J., Martonchik, J. V., Diner, D. J., Crean, K. A., and Holben, B.: Multiangle Imaging Spectroradiometer (MISR) global aerosol optical depth validation based on 2 years of coincident Aerosol Robotic Network (AERONET) observations. J. Geophys. Res., 110, D10S04, doi:10.1029/2004JD004706, 2005.

Kasten, F., and Young, A. T.: Revised optical air mass tables and approximation formula. *Appl. Opt.,* **28**, 4735–4738, 1989.

Kiedron, P., Michalsky, J., Schmid, B., Slater, D., Berndt, J., Harrison, L., Racette, P., Westwater, E., and Han, Y.: A robust retrieval of water vapor column in dry Arctic conditions using the rotating shadowband spectroradiometer. *J. Geophys. Res.*, **106**, 24,007– 24,016, 2001.

Kiedron, P., Berndt, J., Michalsky, J., and Harrison, L.: Column water vapor from diffuse irradiance. *Geophys. Res. Lett.*, **30**(11), 1565, doi:10.1029/2003GL016874, 2003.

Kieffer, H. H.: Photometric stability of the lunar surface. *Icarus*, **130**, 323–327, 1997.

Kieffer, H. H., and Stone, T. C.: The spectral irradiance of the moon. *Astron. J.*, **129**, 2887–2901, 2005.

Kikuchi, M., Murakami, H., Suzuki, K., Nagao, T. M., Higurashi, A.: Improved Hourly Estimates of Aerosol Optical Thickness Using Spatiotemporal Variability Derived From Himawari-8 Geostationary Satellite, *IEEE Trans, Geosci. Remote*

https://doi.org/10.5194/amt-2019-230
Preprint. Discussion started: 5 July 2019

Atmospheric Measurement Techniques Discussions

Sens., **56** (6), 3442-3455, doi: 10.1109/TGRS.2018.2800060, 2018.

Levis, J. R., Campbell, J. R., Welton, E. J., Stewart, S. A., and Phillip C. Haftings, P. C.: Overview of MPLNET version 3 cloud detection, *J. Atmos. Oceanic Technol.*, **33**, 2113–2134, http://dx.doi.org/10.1175/JTECH-D-15-0190.1, 2016.

Lohmann, U., and Feichter, J.: Global indirect aerosol effects: a review. *Atmos. Chem. Phys.*, **5**, 715-737, 2005.

Michalsky, J. J., Liljegren, J. C., and Harrison, L. C.: A comparison of sun photometer derivations of total column water vapor and ozone to standard measures of same at the Southern Great Plains atmospheric radiation measurement site. *J. Geophys. Res.*, **100**, 25,995–26,003, 1995.

Michalsky, J. J., Min, Q., Kiedron, P. W., Slater, D. W., and Barnard, J. C.: A differential technique to retrieve column water vapor using sun radiometry. *J. Geophys. Res.*, **106**, 17,433–17,442, 2001.

Nagasawa, K.: Tentai no ichi keisan (Position calculation of celestial bodies), Chjin Shokan, p. 239, 1981 (in Japanese).

Pappalardo, G., Amodeo, A., Apituley, A., Comeron, A., Freudenthaler, V., Linné, H., Ansmann, A., Bösenberg, J., D'Amico, G., Mattis, I., Mona, L., Wandinger, U., Amiridis, V., Alados-Arboledas, L., Nicolae, D., and Wiegner, M.: EARLINET: towards an advanced sustainable European aerosol lidar network, *Atmos. Meas. Tech.*, **7**, 2389-2409, https://doi.org/10.5194/amt-7-2389-2014, 2014.

Pérez-Ramírez, D., Aceituno, J., Ruiza, B., Olmo, F. J., and Alados-Arboledas, L.: Development and calibration of a star photometer to measure the aerosol optical depth: Smoke observations at a high mountain site. *Atmos. Environ.*, **42**, 2733–2738, 2008.

Perry K. D., Cahill, T. A., Schnell, R. C., and Harris, J. M.: Long-range transport of anthropogenic aerosols to the National Oceanic and Atmospheric Administration baseline station at Mauna Loa Observatory, Hawaii, *J. Geophys. Res.*, **104**, 18,521–18,533, 1999.

Plana-Fattori, A., Legrand, M., Tanre, D., Devaux, C., Vermeulen, A., and Dubuisson, P.: Estimating the atmospheric water vapor content from sun photometer measurements. *J. Appl. Meteorol.*, **37**, 790– 804, 1998.

Plana-Fattori, A., Dubuisson, P., Fomin, B. A., and de Paula Correa, M.: Estimating the atmospheric water vapor content from multi-filter rotating shadow-band radiometry at Sao Paulo, Brazil. *Atmos. Res.*, **71**, 171– 192, 2004.

Prados, A. I., Kondragunta, S., Ciren, P., and Knapp, K. R.: GOES Aerosol/Smoke Product (GASP) over North America: Comparisons to AERONET and MODIS observations. *J. Geophys. Res.*, **112**, D15201, doi:10.1029/2006JD007968, 2007.

https://doi.org/10.5194/amt-2019-230
Preprint. Discussion started: 5 July 2019

Ramanathan, V., Crutzen, P. J., Kiehl, J. T., and Rosenfeld, D.: Aerosols, Climate, and the Hydrological Cycle. *Science*, **294**, 2119-2124, 2001.

Reagan, J. A., Thome, K., Herman, B., and Gall, R.: Water vapor measurements in the 0.94 micron absorption band-Calibration, measurements and data applications. *in Proc. Int. Geoscience and Remote Sensing '87 Symposium, Ann Arbor, Michigan, IEEE,* pp. 63–67, 1987a.

Reagan, J. A., Pilewskie, P. A., Herman, B. M., and Ben-David, A.: Extrapolation of Earth-based solar irradiance measurements to exoatmospheric levels for broad-band and selected absorption-band observations. *IEEE Trans. Geosci. Remote Sens.*, **25**, 647–653, 1987b.

Reagan, J., Thome, K., Herman, B., Stone, R., DeLuisi, J., and Snider, J.: A comparison of columnar water vapor retrievals obtained with near-IR solar radiometer and microwave radiometer measurements. *J. Appl. Meteorol.*, **34**, 1384–1391, 1995.

Remer, L. A., Kaufman, Y. J., Tanré, D., Mattoo, S., Chu, D. A., Martins, J. V., Li, R.-R., Ichoku, C., Levy, R. C., Kleidman, R. G., Eck, T. F., Vermote, E., and Holben, B. N.: The MODIS aerosol algorithm, products and validation. *J. Atmos. Sci.*, **62**, 947–973, https://doi.org/10.1175/JAS3385.1, 2005.

Schmid, B., and Wehrli, C.: Comparison of Sun photometer calibration by use of the Langley technique and the standard lamp, *Appl. Opt.*, **34**, 4500–4512, 1995.

Schmid, B., Thome, K. J., Demoulin, P., Peter, R., Matzler, C., and Sekler, J.: Comparison of modeled and empirical approaches for retrieving columnar water vapor from solar transmittance measurements in the 0.94-μm region. *J. Geophys. Res.*, **101**, 9345–9358, 1996.

Schmid, B., Michalsky, J. J., Slater, D. W., Barnard, J. C., Halthore, R. N., Liljegren, J. C., Holben, B. N., Eck, T. F., Livingston, J. M., Russell, P. B., Ingold, T., and Slutsker, I.: Comparison of columnar water-vapor measurements from solar transmittance methods, *Appl. Opt.*, **40**, 1886–1896, 2001.

Shaw, G. E.: Solar spectral irradiance and atmospheric transmission at Mauna Loa Observatory, *Appl. Opt.*, **21**, 2006–2011, 1982.

Shaw, G. E.: Sun photometry. *Bull. Am. Meteorol. Soc.*, **64**, 4–11, 1983.

Shimizu, A., Nishizawa, T., Jin, Y., Kim, S.-W., Wang, Z., Batdorj, D., Sugimoto, N.: Evolution of a lidar network for tropospheric aerosol detection in East Asia, *Opt. Eng.*, **56**(3), 031219 (2016), doi: 10.1117/1.OE.56.3.031219, 2016.

Shiobara, M., Spinhirne, J. D., Uchiyama, A., and Asano, S.: Optical depth measurements of aerosol, cloud, and water vapor using sun photometers during FIRE Cirrus IFO II. *J. Appl. Meteorol.*, **35**, 36–46, 1996.

https://doi.org/10.5194/amt-2019-230
Preprint. Discussion started: 5 July 2019

Shoji, Y.: Retrieval of Water Vapor Anisotropy using the Japanese Nationwide GPS Array and its Potential for Prediction of Convective Precipitation. *J. Meteor. Soc. Japan*, **91**, 43-62, 2013.

Takamura, T, Nakajima, T., and SKYNET community group: Overview of SKYNET and its Activities. Proceedings of AERONET workshop. *El Arenosillo. Optica Pura y Aplicada,* **37**, 3303–3308, 2004.

Thome, K., Herman, B. M., and Reagan, J. A.: Determination of precipitable water from solar transmission. *J. Appl. Meteorol.*, **31**, 157-165, 1992.

Thome, K. J., Smith, M. W., Palmer, J. M., and Reagan, J. A.: Three-channel solar radiometer for the determination of atmospheric columnar water vapor. *Appl. Opt.*, **33**, 5811 –5819, 1994.

Uchiyama, A., Yamazaki, A., Kudo, R.: Column Water Vapor Retrievals from Sky-radiometer (POM-02) 940nm Data. *J. Meteorol. Soc. Japan*, **92A**, 195-203, DOI:10.2151/jmsj.2014-A13, 2014.

Uchiyama, A., Matsunaga, T., and Yamazaki, A.: The instrument constant of sky radiometers (POM-02) – Part 1: Calibration constant, *Atmos. Meas. Tech.*, **11**, 5363-5388, https://doi.org/10.5194/amt-11-5363-2018, 2018.

Wang, M., Bailey, S., and McClain, C. R.: SeaWiFS provides unique global aerosol optical property data. *Eos, Trans. Amer. Geophys. Union*, **81**, 197–202, 2000.

World Health Organisation: WHO Air quality guidelines for particulate matter, ozone, nitrogen dioxide and sulfur dioxide; Global update 2005; Summary of risk assessment. World Health Organization, Geneva, Switzerland, p. 22, 2006.

World Health Organization Regional Office for Europe: Review of Evidence on Health Aspects of Air Pollution–REVIHAAP Project, Technical Report WHO, Copenhagen, p. 298, 2013.

Wehrli, C.: GAW–PFR: A network of Aerosol Optical Depth observations with Precision Filter Radiometers. In: WMO/GAW Experts workshop on a global surface based network for long term observations of column aerosol optical properties, Tech. rep., GAW Report No. 162, WMO TD No. 1287, ftp://ftp.wmo.int/Documents/PublicWeb/arep/gaw/gaw162.pdf, 2005.

Welton, E. J., Campbell, J. R., Spinhirne, J. D., and Scott, V. S.: Global monitoring of clouds and aerosols using a network of micro-pulse lidar systems. *Lidar Remote Sensing for Industry and Environmental Monitoring*, U. N. Singh, T. Itabe, and N. Sugimoto, Eds., International Society for Optical Engineering (SPIE Proceedings, Vol. 4153), 151–158, 2001.

Winker, D. M., Hunt, W. H., and McGill, M. J.: Initial performance assessment of CALIOP. Geophys. *Res. Lett.*, **34**, L19803, doi:10.1029/2007GL030135, 2007.

https://doi.org/10.5194/amt-2019-230
Preprint. Discussion started: 5 July 2019

Atmospheric Measurement Techniques
Discussions

Yokota, Y., Matsunaga, T., Ohtake, M., Haruyama, J., Nakamura, R., Yamamoto, S., Ogawa, Y., Morota, T., Honda, C., Saiki, K., Nagasawa, K., Kitazato, K., Sasaki, S., Iwasaki, A., Demura, H., Hirata, N., Hiroi, T., Honda, R., Iijima, Y., Mizutani, H.: Lunar photometric properties at wavelengths 0.5–1.6 μm acquired by SELENE Spectral Profiler and their dependency on local albedo and latitudinal zones, *Icarus*, **215**, 639-660, 2011.

Yoshida, M., Kikuchi, M., Nagao, T. M., Murakami, H., Nomaki, T., Higurashi, A.: Common Retrieval of Aerosol Properties for Imaging Satellite Sensors, *J. Meteorol. Soc. Jpn.*, **96B**, 193-209, doi: 10.2151/jmsj.2018-039, 2018.

Table 1 Examples of calibration coefficient V_{S0} for the solar measurement

Table 2 Measurement range before (current) and after modification (new) of POM-02. I_n and I_{n-1} are the upper and lower limit current (unit: A), respectively.

Table 3 Coefficients of the regression equation for reflectance correction factor C

Table 4 Results of comparison between NIES/HSRL and POM-02 aerosol optical depth

Table 5 Same as Table 4 except for radiosonde and POM-02 precipitable water vapor

Table 6 Same as Table 4 except for radiosonde and corrected POM-02 precipitable water vapor.

Table 7 Same as Table 4 except for GPS and radiosonde precipitable water vapor.

Table 8 Same as Table 4 except for GPS and corrected POM-02 precipitable water vapor.

Figure captions

Fig. 1 An example of sensor output for the solar direct irradiances and the scattered sky radiances by POM-02.

Fig. 2 Examples of Langley plot in the visible and near-infrared region.

Fig. 3 Examples of Langley plot in the shortwave infrared region.

https://doi.org/10.5194/amt-2019-230
Preprint. Discussion started: 5 July 2019

Fig. 4 Relationship between phase angle and reflectance correction factor $C = V_{m0} / V_{S0}$ in the visible and near-infrared region. A regression curve ($C = A_c \cdot g^2 + B_c$, g : Phase angle) was also plotted.

Fig. 5 Relationship between phase angle and reflectance correction factor $C = V_{m0} / V_{S0}$ in the shortwave infrared region. A regression curve ($C = A_c \cdot g^2 + B_c$, g : Phase angle) was also plotted.

Fig. 6 Scatter plot of HSRL and POM-02 aerosol optical depth. (a) daytime (red), (b) nighttime (blue), (c) overlapping daytime (red) with nighttime (blue).

Fig. 7 Examples of time series of HSRL (red), POM-02 daytime (green) and nighttime (blue) aerosol optical depths.

Fig. 8 Scatter plot of Radiosonde and POM-02 precipitable water vapor. daytime is red symbol, and nighttime is blue one.

Fig. 9 Same as Fig. 8 except for corrected POM-02 precipitable water vapor.

Fig. 10 Scatter plot of GPS and Radiosonde precipitable water vapor.

Fig. 11 Scatter plot of PWV from GPS and corrected PWV from POM-02. (a) daytime (red), (b) nighttime (blue), (c) overlapping daytime (red) with nighttime (blue).

Fig. 12 Examples of time series of GPS (red), POM-02 daytime (green) and nighttime (blue) corrected precipitable water vapor.

https://doi.org/10.5194/amt-2019-230
Preprint. Discussion started: 5 July 2019

Atmospheric Measurement Techniques Discussions

Table 1 Examples of calibration coefficient V_{S0} for the solar measurement

Wavelength (nm)	340	380	400	500	675	870	940	1020
V_{S0} ($\times 10^{-4}$)	0.1799	0.1882	1.603	3.174	3.444	2.299	1.055	1.077

Wavelength (nm)	1225	1627	2200
V_{S0} ($\times 10^{-4}$)	0.9305	1.321	0.7873

Table 2 Measurement range before (current) and after modification (new) of POM-02. I_n and I_{n-1} are the upper and lower limit current (unit: A), respectively.

		Current			New		
1	$I_1 - I_2$	2.5×10^{-3}	–	2.5×10^{-4}	2.5×10^{-3}	–	1.25×10^{-4}
2	$I_2 - I_3$	2.5×10^{-4}	–	2.5×10^{-5}	1.25×10^{-4}	–	6.25×10^{-6}
3	$I_3 - I_4$	2.5×10^{-5}	–	2.5×10^{-6}	6.25×10^{-6}	–	3.125×10^{-7}
4	$I_4 - I_5$	2.5×10^{-6}	–	2.5×10^{-7}	3.125×10^{-7}	–	1.5625×10^{-8}
5	$I_5 - I_6$	2.5×10^{-7}	–	2.5×10^{-8}	1.5625×10^{-8}	–	7.8125×10^{-10}
6	$I_6 - I_7$	2.5×10^{-8}	–	2.5×10^{-9}	7.8125×10^{-10}	–	3.90625×10^{-11}
7	I_7	2.5×10^{-9}	–	0.0	3.90625×10^{-11}	–	0.0
	I_n	$I_n=I_{n-1}/10$			$I_n=I_{n-1}/20$		

Table 3 Coefficients of the regression equation for reflectance correction factor C

Wavelength (nm)	A_c	B_c
340	1.3404×10^{-5}	0.98027
380	1.3512×10^{-5}	1.0674
400	3.0760×10^{-6}	1.0058
500	2.2487×10^{-6}	1.1600
675	4.8644×10^{-6}	1.0840
870	3.4967×10^{-6}	1.0855
940	7.2405×10^{-8}	1.1532
1020	6.7912×10^{-6}	1.0559
1225	9.0288×10^{-5}	1.0572
1627	2.3828×10^{-5}	1.0810
2200	3.7545×10^{-5}	0.95311

$C = A_c \cdot g^2 + B_c$, g: phase angle (degrees)

https://doi.org/10.5194/amt-2019-230
Preprint. Discussion started: 5 July 2019

Table 4 Results of comparison between NIES/HSRL and POM-02 aerosol optical depth

POM-02	Bias	RMSE	CR	C_1	C.I. of C_1 (95%)	C_2	C.I. of C_2 (95%)	RMSE of reg.	NO of obs.
Sun+Moon	0.0437	0.0839	0.8266	0.9611	±0.0295	0.0486	±0.0049	0.0715	1889
Sun	0.0432	0.0866	0.7650	0.8877	±0.0425	0.0573	±0.0068	0.0743	1192
Moon	0.0466	0.0838	0.8825	1.0477	±0.0414	0.0405	±0.0074	0.0694	702

RMSE: Root mean square error

CR: Correlation coefficient

C_1 and C_2 : coefficients of regression line ($\tau_{HSRL} = C_1 \cdot \tau_{POM-02} + C_2$)

C.I. of C_1 (95%): 95% confidential interval of C_1

C.I. of C_2 (95%): 95% confidential interval of C_2

RMSE of reg.: RMSE of regression line

Table 5 Same as Table 4 except for radiosonde and POM-02 precipitable water vapor

POM-02	Bias	RMSE	CR	C_1	C.I. of C_1 (95%)	C_2	C.I. of C_2 (95%)	RMSE of reg.	No. of obs.
Sun+Moon	−0.2477	0.3037	0.9946	0.7948	±0.0138	−0.0057	±0.0196	0.0658	141
Sun	−0.2206	0.2764	0.9945	0.8041	±0.0165	−0.0044	±0.0223	0.0661	104
Moon	−0.3259	0.3726	0.9966	0.7811	±0.0214	−0.0212	±0.0343	0.0508	37

PWV, Bias, RMSE, RMSE of reg.: g/cm²

C_1 and C_2: coefficients of regression line ($PWV_{POM-02} = C_1 \cdot PWV_{Sonde} + C_2$).

Table 6 Same as Table 4 except for radiosonde and corrected POM-02 precipitable water vapor.

POM-02	Bias	RMSE	CR	C_1	C.I. of C_1 (95%)	C_2	C.I. of C_2 (95%)	RMSE of reg.	No. of obs.
Sun+Moon	−0.0027	0.0830	0.9946	1.0042	±0.0173	−0.0077	±0.0246	0.0829	142
Sun	0.0115	0.0848	0.9945	1.0160	±0.0206	−0.0061	±0.0278	0.0831	105
Moon	−0.0454	0.0794	0.9966	0.9869	±0.0271	−0.0272	±0.0434	0.0643	37

C_1 and C_2 : coefficients of regression line ($PWV_{POM-02}(corrected) = C_1 \cdot PWV_{Sonde} + C_2$).

https://doi.org/10.5194/amt-2019-230
Preprint. Discussion started: 5 July 2019

Atmospheric Measurement Techniques Discussions
Open Access

Table 7 Same as Table 4 except for GPS and radiosonde precipitable water vapor.

Sonde	Bias	RMSE	CR	C_1	C.I. of C_1 (95%)	C_2	C.I. of C_2 (95%)	RMSE of reg.	No. of obs.
Sonde	0.0770	0.2229	0.9791	0.9425	±0.0233	0.1572	±0.0403	0.2007	274

C_1 and C_2: coefficients of regression line ($PWV_{Sonde} = C_1 \cdot PWV_{GPS} + C_2$).

Table 8 Same as Table 4 except for GPS and corrected POM-02 precipitable water vapor.

POM-02	Bias	RMSE	CR	C_1	C.I. of C_1 (95%)	C_2	C.I. of C_2 (95%)	RMSE of reg.	No. of obs.
Sun+Moon	0.0159	0.2050	0.9664	0.9032	±0.0089	0.1255	±0.0122	0.1896	2826
Sun	0.0072	0.1939	0.9706	0.9056	±0.0097	0.1164	±0.0137	0.1787	2046
Moon	0.0391	0.2232	0.9527	0.9132	±0.0221	0.1292	±0.0279	0.2106	671

C_1 and C_2: coefficients of regression line ($PWV_{POM-02}(corrected) = C_1 \cdot PWV_{GPS} + C_2$).

https://doi.org/10.5194/amt-2019-230
Preprint. Discussion started: 5 July 2019

Atmospheric Measurement Techniques Discussions

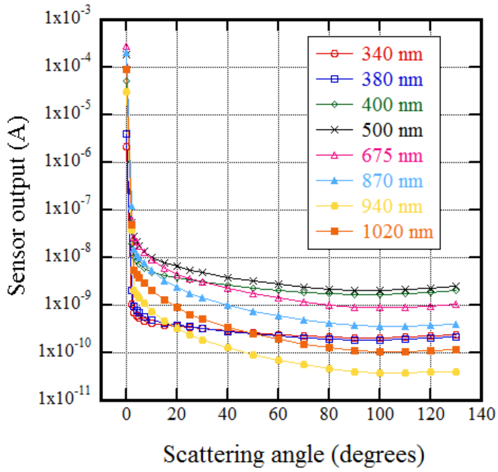

Fig. 1 Examples of sensor output for solar direct irradiances and scattered sky radiances from POM-02.

https://doi.org/10.5194/amt-2019-230
Preprint. Discussion started: 5 July 2019

Atmospheric Measurement Techniques Discussions

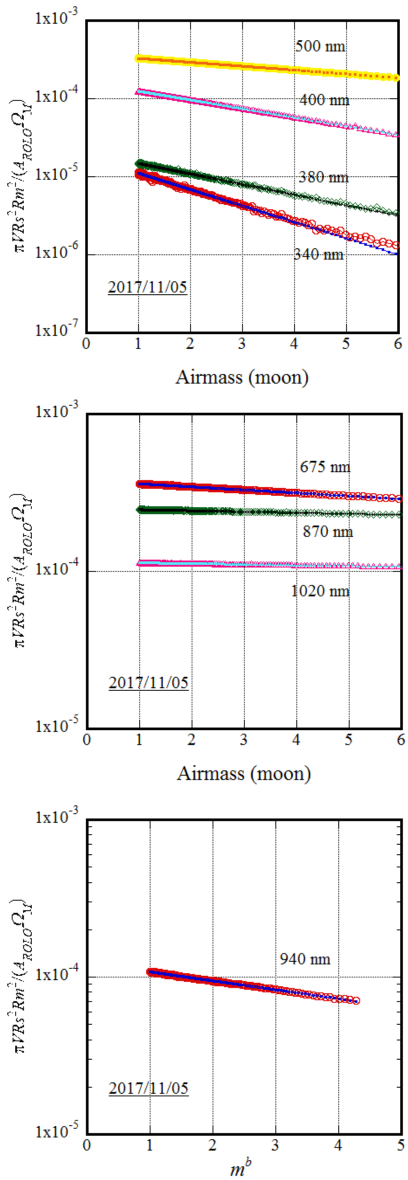

Fig. 2 Examples of a Langley plot in the visible and near-infrared region.

https://doi.org/10.5194/amt-2019-230
Preprint. Discussion started: 5 July 2019

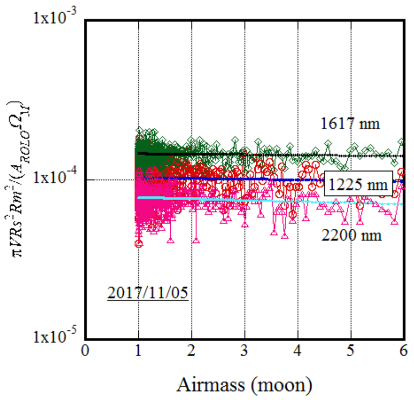

Fig. 3 Examples of Langley plots in the shortwave infrared region.

https://doi.org/10.5194/amt-2019-230
Preprint. Discussion started: 5 July 2019

Atmospheric Measurement Techniques
Discussions

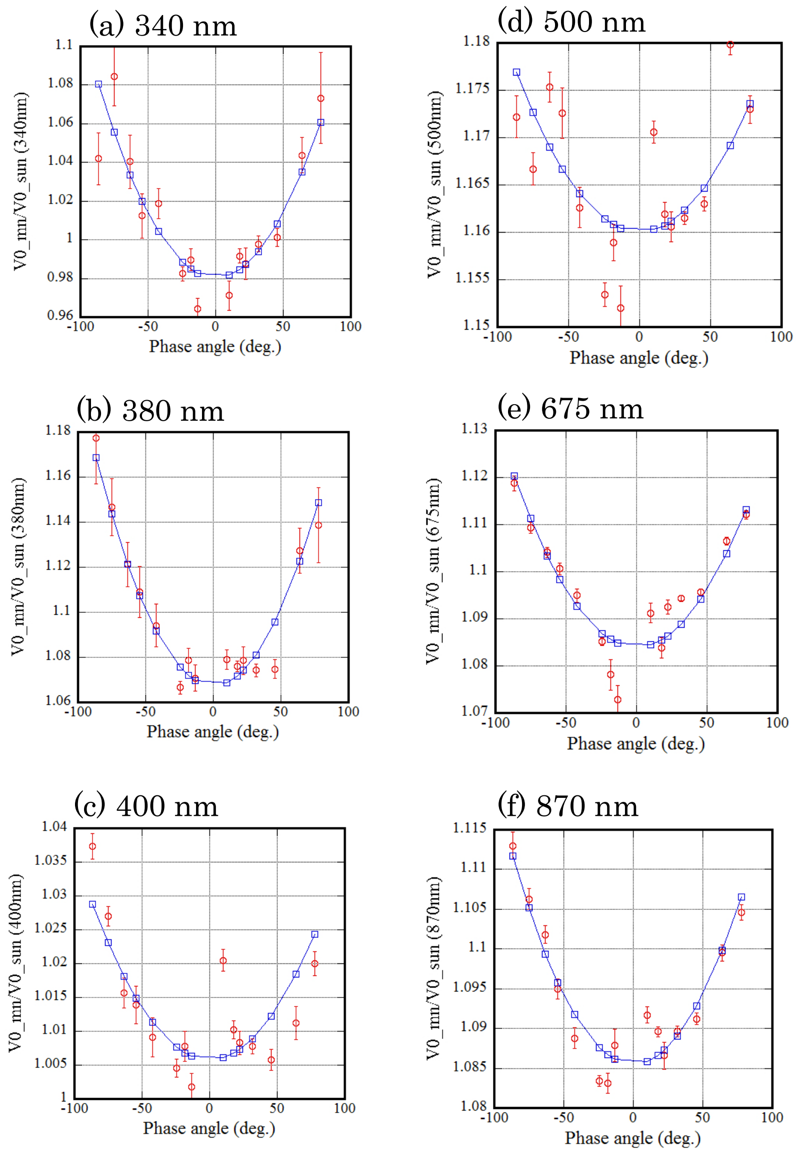

Fig. 4 to be continued.

https://doi.org/10.5194/amt-2019-230
Preprint. Discussion started: 5 July 2019

Atmospheric Measurement Techniques
Discussions

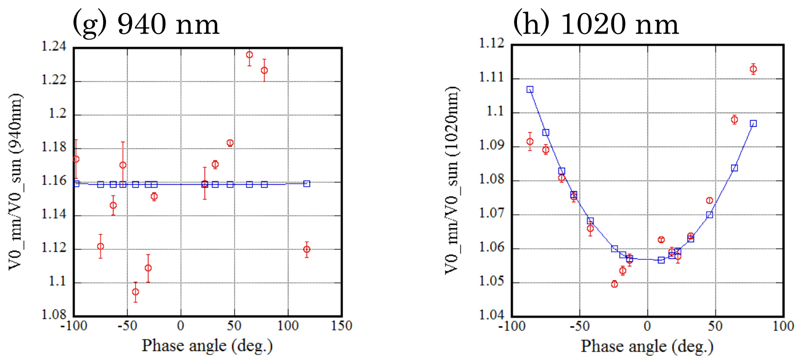

Fig. 4 Relationship between phase angle and reflectance correction factor $C = V_{m0} / V_{S0}$ in visible and near-infrared region. A regression curve ($C = A_c \cdot g^2 + B_c$, g : Phase angle) was also plotted.

to be continued.

https://doi.org/10.5194/amt-2019-230
Preprint. Discussion started: 5 July 2019

Atmospheric Measurement Techniques
Discussions
Open Access

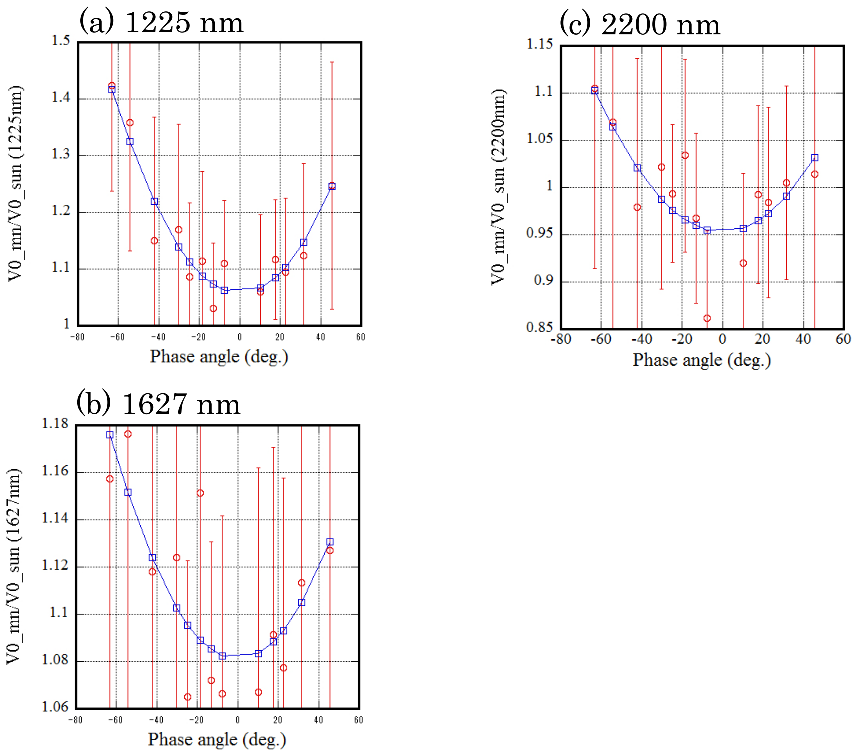

Fig. 5 Relationship between phase angle and reflectance correction factor $C = V_{m0} / V_{S0}$ in shortwave infrared region. A regression curve ($C = A_c \cdot g^2 + B_c$, g : Phase angle) was also plotted.

https://doi.org/10.5194/amt-2019-230
Preprint. Discussion started: 5 July 2019

Atmospheric Measurement Techniques
Discussions

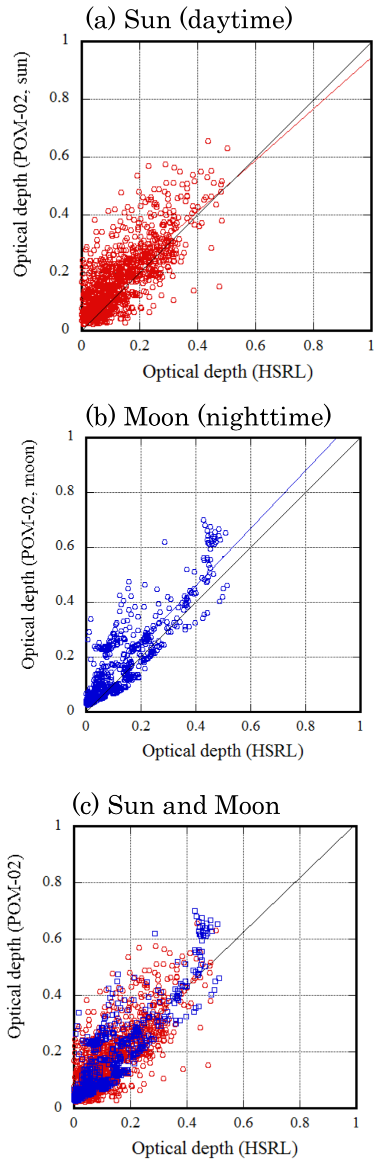

Fig. 6 Scatter plot of NIES/HSRL and POM-02 aerosol optical depth. (a) Daytime (red), (b) nighttime (blue), (c) overlapping daytime (red) with nighttime (blue).

https://doi.org/10.5194/amt-2019-230
Preprint. Discussion started: 5 July 2019

Atmospheric Measurement Techniques Discussions
Open Access
EGU

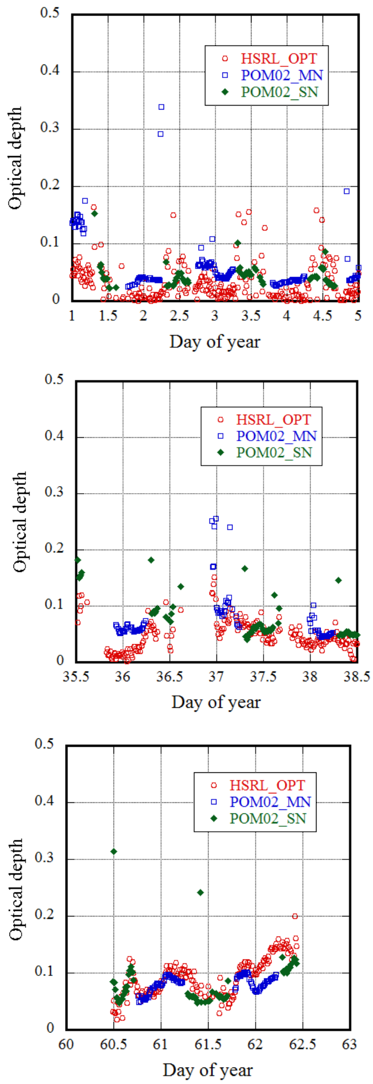

Fig. 7 Examples of time series of NIES/HSRL (red), POM-02 daytime (green), and nighttime (blue) aerosol optical depths.

https://doi.org/10.5194/amt-2019-230
Preprint. Discussion started: 5 July 2019

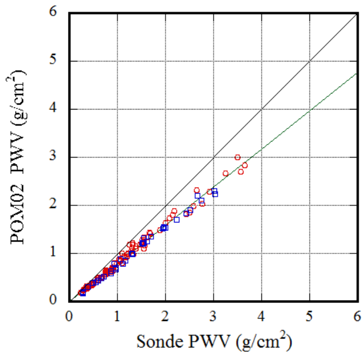

Fig. 8 Scatter plot of radiosonde and POM-02 precipitable water vapor. Daytime (nighttime) observations are indicated by red (blue) symbols.

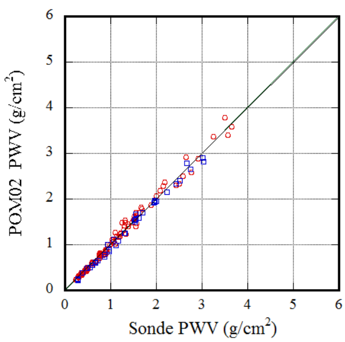

Fig. 9 Same as Fig. 8 except for corrected POM-02 precipitable water vapor.

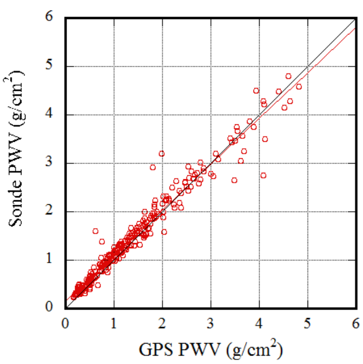

Fig. 10 Scatter plot of GPS and radiosonde precipitable water vapor.

https://doi.org/10.5194/amt-2019-230
Preprint. Discussion started: 5 July 2019

Atmospheric Measurement Techniques Discussions

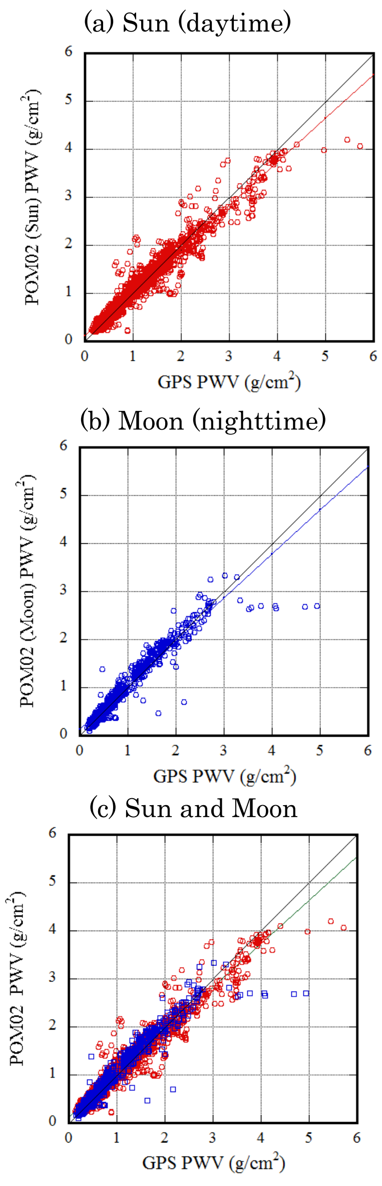

Fig. 11 Scatter plot of PWV from GPS and corrected PWV from POM-02. (a) Daytime (red), (b) nighttime (blue), (c) overlapping daytime (red) with nighttime (blue).

https://doi.org/10.5194/amt-2019-230
Preprint. Discussion started: 5 July 2019

Atmospheric Measurement Techniques Discussions

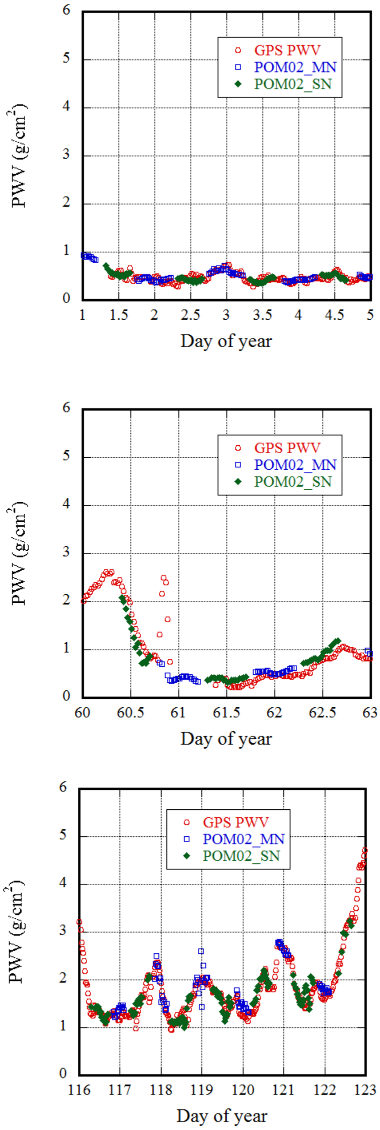

Fig. 12 Examples of time series of GPS (red), POM-02 daytime (green), and nighttime (blue) corrected precipitable water vapor.